PHYSICAL REVIEW D VOLUME 16, NUMBER 11 1 DECEMBER 1977

Study of neutrino interactions in hydrogen and deuterium: Description of the experiment and study of the reaction $\nu + d \to \mu^- + p + p_s$ †

S. J. Barish,* J. Campbell,‡ G. Charlton,§ Y. Cho, M. Derrick, R. Engelmann,‖ L. G. Hyman, D. Jankowski, A. Mann,¶ B. Musgrave, P. Schreiner, P. F. Schultz, R. Singer, M. Szczekowski,** T. Wangler, and H. Yuta††
Argonne National Laboratory, Argonne, Illinois 60439

V. E. Barnes, D. D. Carmony, A. F. Garfinkel, and G. M. Radecky
Purdue University, Lafayette, Indiana 47907

(Received 30 June 1977)

This paper gives a detailed description of an experiment which studies the interactions of muon-type neutrinos in hydrogen and deuterium. The experiment was performed at the Zero Gradient Synchrotron using the wide-band neutrino beam incident on the Argonne 12-foot bubble chamber filled with hydrogen and deuterium. The neutrino energy spectrum peaks at 0.5 GeV and has a tail extending to 6 GeV. The shape and intensity of the flux is determined using measurements of pion yields from beryllium. The produced pions are focused by one or (for the latter part of the experiment) two magnetic horns. A total of 364000 pictures were taken with a hydrogen filling of the bubble chamber and 903000 with a deuterium filling. The scanning and other analyses of the events are described. The most abundant reaction occurs off neutrons and is quasi-elastic scattering $\nu d \to \mu^- p p_s$. The separation of these events from background channels is discussed. The total and differential cross sections are analyzed to obtain the axial-vector form factor of the nucleon. Our result, expressed in terms of a dipole form factor, gives an axial-vector mass of 0.95 ± 0.09 GeV. A comparison is made to previous measurements using neutrino beams, and also to determinations based upon threshold pion electroproduction experiments. In addition, the data are used to measure the weak vector form factor and so check the conserved-vector-current hypothesis.

I. INTRODUCTION

The experimental study of neutrino interactions started more than twenty years ago with the observation of inverse β decay by Reines and Cowan.[1] The realization that a weak-interaction cross section increasing with energy would allow experiments to be carried out using neutrinos coming from pion decay, now called muon neutrinos ν_μ, occurred to several people in the late 1950's.[2] These considerations resulted in the first observation[3] of the interactions of high-energy neutrinos with complex nuclei at the Brookhaven National Laboratory in 1962 and to the discovery of the existence of two neutrinos, the electron neutrino (ν_e), and the muon neutrino (ν_μ). Further experiments were done at several laboratories using spark-chamber detectors,[4] but much of the additional information came from experiments using a small bubble chamber filled with Freon.[5] This detector was operated at the CERN proton synchrotron and allowed the first crude studies of the properties of the hadronic system resulting from $\nu_\mu N$ interactions in the (1–2)-GeV energy range. Later, the chamber was enlarged and filled with propane, allowing events of single-pion production from a free proton target to be analyzed.[6]

Following these experiments, it became clear that refinements of the technique were necessary to further understand the details of the interactions. At CERN, a much larger heavy-liquid bubble chamber called Gargamelle[7] was brought into use. This detector gave event rates as high as ~1 event per 20 expansions and also provided both better muon identification and more accurate hadronic energy measurements than had previously been possible. With Gargamelle, the characteristics of inclusive ν and $\bar{\nu}$ nucleon interactions were well measured, giving clear evidence for the quark-parton structure of the nucleon.[8]

We have followed another approach by using pure targets of hydrogen and deuterium in a 12-foot-diameter bubble chamber exposed to the ν_μ beam at the Zero Gradient Synchrotron (ZGS) of Argonne National Laboratory. This use of a simple target allows the best measurement of the nucleon form factors.[9] Since the ν_μ flux, resulting from the decay of pions produced by 12.4-GeV protons peaks at about 0.5 GeV, one can also study the threshold behavior of single- and double-pion production.[10-12]

In particular, by using both hydrogen and deuterium fillings of the chamber, one can study pion production in different charge states and so isolate the isospin $\frac{1}{2}$ and $\frac{3}{2}$ contributions to the final-state hadronic system.[11] The total cross sections for $\nu_\mu n$ and $\nu_\mu p$ interactions near threshold provide separate constraints on the quark-parton picture of the nucleon[12] and cast light on the question of precocious scaling that had been seen in the Gargamelle data.

The discovery of neutral-current (NC) interactions in which the emerging lepton is also a neutrino has opened up a new chapter of weak-interaction physics.[13] Investigations of the simple NC reactions such as $\nu p \rightarrow \nu p$ and single-pion production $\nu n \rightarrow \nu p \pi^-$, $\nu p \rightarrow \nu p \pi^0$, $\nu p \rightarrow \nu n \pi^+$ are most important in elucidating the nature of the NC interaction.[14]

The present paper contains a general description of the neutrino experiment in the 12-foot bubble chamber, including a discussion of the flux measurements. The analysis methods used to extract the data are briefly described. Finally, we discuss the cross-section measurements of the quasi-elastic reaction $\nu d \rightarrow \mu^- p p_s$ and their analysis in terms of the nucleon form factors. In a second paper, the results on single- and multiple-pion production by the charged current will be given. The results of the NC events will be discussed in a third paper.

II. DESCRIPTION OF THE NEUTRINO BEAM

The neutrino beam at the ZGS is shown in Fig. 1. The 12.4-GeV/*c* circulating protons in the accelerator are extracted, transported through the external-proton-beam experimental area II along beam line 9 and focused onto a beryllium target placed near the face of the first focusing horn.[15] Beam 46 provides a K_L^0 beam to the bubble chamber. During operation for the neutrino experiment, the first elements of beam 46 are moved to one side to allow a free decay tunnel. The present beam arrangement has a second horn placed just downstream of the first horn. The second focusing device was only used during the latter part of this experiment. The produced positive (negative) pions are focused (defocused) by these devices and directed towards the bubble chamber. The pions decay in the ~30-m-long drift space, which is a tunnel surrounded by concrete and steel. A steel and lead shield ~15 m long before the bubble chamber removes hadrons and charged leptons, allowing the pure neutrino beam to enter the bubble-chamber liquid.

The spot size of the extracted proton beam on the face of the target was about 3 mm in diameter and so is smaller than the target which was a beryllium rod, 61 cm long, tapering from a diameter of 1.59 cm at the upstream end to 2.22 cm at the downstream end. The position and size of the proton beam spot were measured every ZGS pulse using segmented wire ion chambers. Typical variations in the position of the spot were ±0.5 mm horizontally and ±0.1 mm vertically with smaller variations in the size. Periodically throughout each run, a glass plate was mounted directly on the upstream face of the target for a few ZGS pulses, and the position and size of the proton beam spot visually measured through the darkening of the glass. The alignment of the proton beam with the axis of the target and first horn was checked at the beginning of a run by using additional glass plates on the downstream end of the target and each horn. Subsequent to a run, the distribution of radioactivity throughout the Be of the target was measured by the intensity of the 480-keV γ line resulting from the $^7\text{Be} \rightarrow {}^7\text{Li}^* \rightarrow {}^7\text{Li} + \gamma$ decay sequence. This activity measurement allowed a check to be made that the proton beam was contained within the target throughout the run.

The intensity of the proton beam [typically $(1.0-1.8) \times 10^{12}$ protons per pulse] was measured

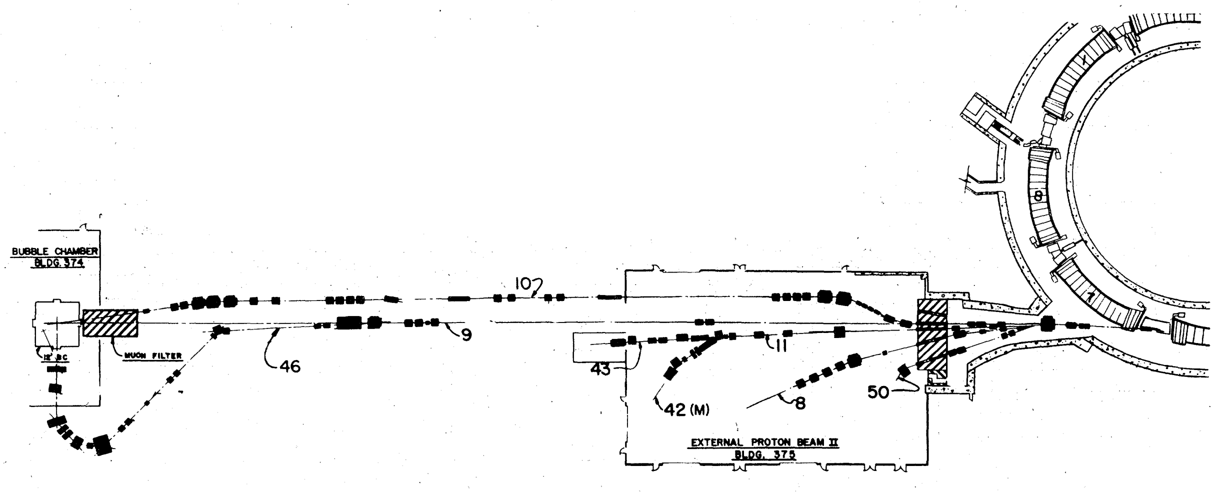

FIG. 1. Beam arrangement of the ZGS neutrino experiment. The 12.4-GeV/*c* proton beam is extracted and transported along beam 9 to the neutrino target. Following a drift space, all hadrons and charged leptons are removed by the muon filter. The shielding is not shown.

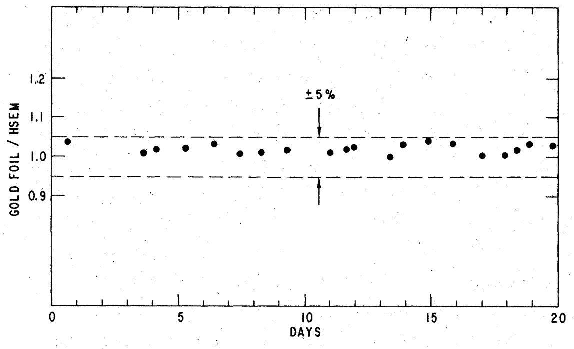

FIG. 2. Ratio of proton beam intensity as measured by activation of a gold foil and the secondary-emission monitor (HSEM) placed just before the target for a three-week exposure of the bubble chamber.

by using a toroidal coil operated as a transformer and placed just before the target. The proton beam had a gross time duration of 10 to 15 μsec, so that a 100-μsec integrating time of the toroid pulse was used to measure the charge. Periodically, a gold foil was exposed to the proton beam and the intensity checked by measurement of the ^{149}Tb α activity.[16] This can be done to a relative accuracy of 2%. In addition to these two absolute measurements of the proton-beam intensity, a secondary-emission monitor (SEM) was used to give a relative measurement. The three different techniques typically tracked throughout a four-week run to within a few percent. This is illustrated in Fig. 2, where we show the ratio of the proton-beam intensity as measured by the gold-foil method to that measured using the SEM over a 21-day period. Similar small variations were obtained in the other exposures.

A scintillation-counter telescope viewing the target at a backward angle and two Čerenkov counters placed in the muon shield also gave digital measurements proportional to the proton and neutrino beam intensity, respectively. Because of the short beam pulse, these counters were arranged to give only 10–20 counts per pulse and would typically have accidental rates of 20%. The readings of all these monitors, together with other data such as the values of the currents in each of the focusing horns and the size and position of the proton beam spot were written on an incremental magnetic tape every pulse using a Xerox Data Systems Sigma 2 computer.

Figure 3 shows the details of the target and focusing horns. The first horn is transformer-coupled to a high-inductance primary resulting in a half-sine-wave current form with a base length of 4 msec. The current in the second horn is directly fed from the capacitor bank, and the base pulse length is 150 μsec. For typical running conditions, the horn currents were 230 kA although lower current values were used on occasions. With these currents the magnetic field in the first horn varied from 25.5 kG at the narrowest part of the neck near the target to 1.1 kG at the outer radius. In the second horn, the equivalent values are 4.8 kG and 0.84 kG.

By varying the currents in the horns and the position of the target along the beam direction, one can change the shape of the neutrino spectrum slightly. The target position and horn currents were chosen to maximize the event rate in the hydrogen exposure, which in effect means maximizing the number of $\nu_\mu p \to \mu^- p \pi^+$ events.

The neutrino flux is calculated by using data on cross sections for pion production in p-Be colli-

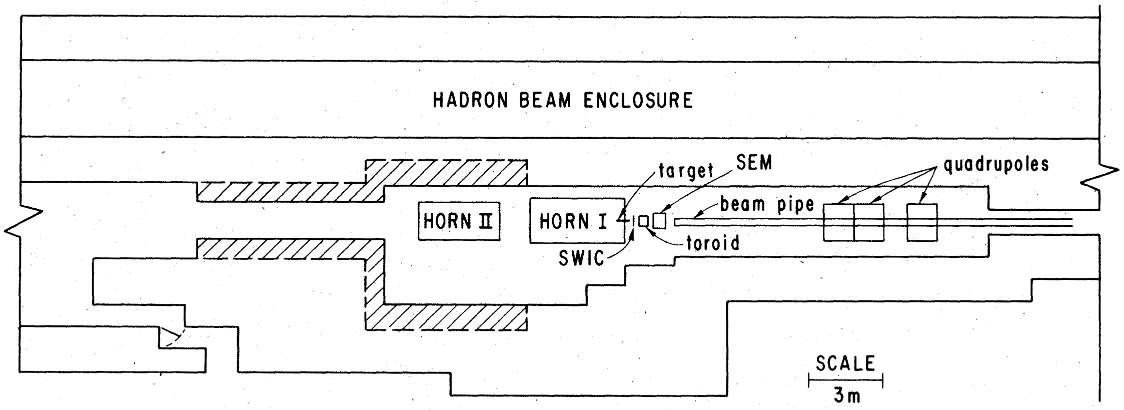

FIG. 3. Detail of placement of the focusing horns and beam monitoring equipment. The steel (shaded) and concrete shielding is shown.

sions at 12.4 GeV/*c*, which were measured in a separate experiment.[17] The measurements were made over the pion momentum range from 2 to 6 GeV/*c* and from 0° to 12° in production angle using 2-cm and 5-cm-long Be discs as targets. Other measurements at 3°, 12°, and 15° were also used.[18] These cross-section measurements, which have a typical precision of ±5%, were fitted to the expression developed by Sanford and Wang[19]

$$\frac{d^2\sigma}{d\Omega dp}=C_1p^{C_2}\left(1-\frac{p}{p_B-1}\right)\times\exp\left[-\frac{C_3p^{C_4}}{p_B{}^{C_5}}-C_6\theta(p-C_7p_B\cos^{C_8}\theta)\right],\tag{1}$$

where $d^2\sigma/d\Omega dp$ is the differential particle yield per interacting proton, the C's are constants found by fitting the yield data, θ is the laboratory production angle (radians), and p and p_B are the momenta (GeV/*c*) of the secondary and incident particles, respectively. The factor $1-p/(p_B-1)$ is used to ensure that the cross section falls to zero at the kinematic limit. The C values so determined are the following: $C_1=196$, giving the cross section in mb, $C_2=1.08$, $C_3=2.15$, $C_4=2.31$, $C_5=1.98$, $C_6=5.73$, $C_7=0.137$, and $C_8=24.1$. This equation was used as the basic pion-production generator. These data and the fits using Eq. (1) are shown in Fig. 4.

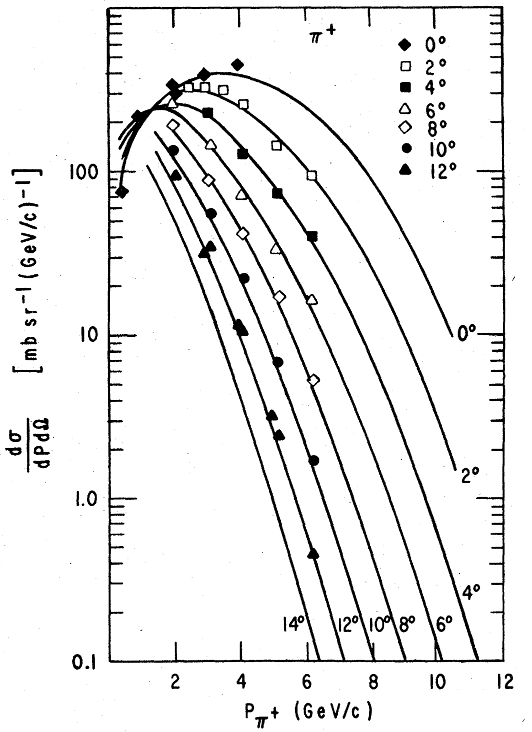

FIG. 4. Cross sections for π^+ production from p-Be collisions at 12.4 GeV/*c*.

Since the same gold-foil activation technique was used for measuring the proton beam intensity, and in normalizing the pion production data, as was used during the neutrino runs, the absolute Tb^{149} production-cross-section uncertainty of 8% does not enter into the ν_μ flux uncertainty. For this reason and since the gold-foil measurements track well with both the toroid and the SEM, we have used the gold-foil data as our absolute measure of the proton beam intensity. In comparing our yield data with the measurements of Allaby *et al.* at 19 GeV,[20] we found good agreement with the shape but a 10% discrepancy in absolute normalization. This is well within the relative errors of the different normalization techniques used.

In order to convert the thin-target cross-section measurements to pion yields from a thick target in the experimental setup, several other effects must be taken into account. They are, first, the attenuation of the proton beam in passing through the target, second, the absorption of the produced pions by the target and other material such as the skins of the horns, and third, the secondary production of pions by pions and protons originating in the initial collision.

The number of pions (n) coming from a thick target of length L can be written as

$$n\propto\frac{N_p\sigma_\pi}{1/\lambda_\pi-1/\lambda_p}\left(e^{-L/\lambda_p}-e^{-L/\lambda_\pi}\right),\tag{2}$$

where λ_p and λ_π are the proton and pion attentuation lengths, σ_π is the pion production cross section, and N_p is the number of incident protons. Since only two target lengths were used, σ_π, λ_π, and λ_p cannot be separately measured. Fitting our 2-cm and 5-cm target data to this expression, one obtains a relationship between λ_p and λ_π such that the yield measurements give the same production cross sections.

For the individual π and p cross sections on nucleons, λ_π and λ_p are quite different with $\lambda_\pi \sim 1.5\lambda_p$ at high energy. In a heavy nucleus, however, where the nuclear diameter is greater than the mean free path in nuclear matter $\lambda_\pi \sim \lambda_p$. Beryllium is between these limits in that it is a small nucleus. Using other measurements of absorption cross sections[21] and the λ_π, λ_p relation determined from our yield data, we chose a value of 42.0 cm for λ_p and 48.0 cm for λ_π in Be. We use $\lambda_\pi=48.0$ cm for the absorption length in the Al skin of the horns.

The secondary production of high-energy pions by pions is negligible because of the rapid fall of the cross sections with energy and angle as seen in Fig. 4. The proton production at small angles, however, gives a nearly flat cross section with momentum as shown by the data of Lundy *et al.*[22]

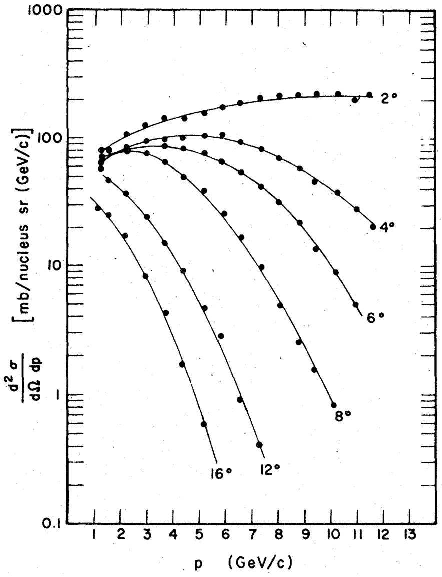

FIG. 5. Cross sections for proton production in p-Be collisions at 12.4 GeV/c from Ref. 22. The absolute normalization of these data is too high by a factor of about 1.5.

in Fig. 5. This leading-particle effect means that pion production from secondary protons is a significant effect and increases the production of low-momentum pions. We estimate these effects by using Eq. (1) and extrapolating to lower proton beam energies, using the data of Fig. 5 to give the number of lower-energy protons produced.

We did not measure the kaon production in our yield experiment. Such sketchy data as exist[19,22] suggest that using a K^+/π^+ ratio of 0.1 and scaling the pion production affords a reasonable approximation to kaon production.

The charged particles produced are allowed to pass through the focusing horns and to decay in the drift space to give the neutrino beam. The resulting beam is spread both in momentum and position as shown in Fig. 6, which gives the normalized profiles of intensity per unit area at the bubble chamber for different ν_μ energies. At the highest energies, the flux is spread over an area smaller than the bubble chamber, whereas for the lowest energies the beam is much larger than the detector.

The useful flux is that contained within the fiducial volume of the bubble chamber, and we show in Figs. 7(a) and 7(b) the different contributions to the flux for the single-horn and two-horn beam, respectively. The units are cm of H_2 or D_2 traversed by the neutrinos using the real shape of the fiducial volume of the bubble chamber. The relative contributions from the kaons and pions produced by secondary protons are shown dotted in Fig. 7(b). It is clear that the flux resulting from the pions, whose production cross section was directly measured, dominates between 0.5 and 2.5 GeV. The $\bar{\nu}_\mu$ flux coming from the defocused negative particles was calculated in the same way as for the wanted ν_μ flux and is shown in Fig. 7(c). We used the measured π^- yields[17] and a K^-/π^- ratio of 2%.

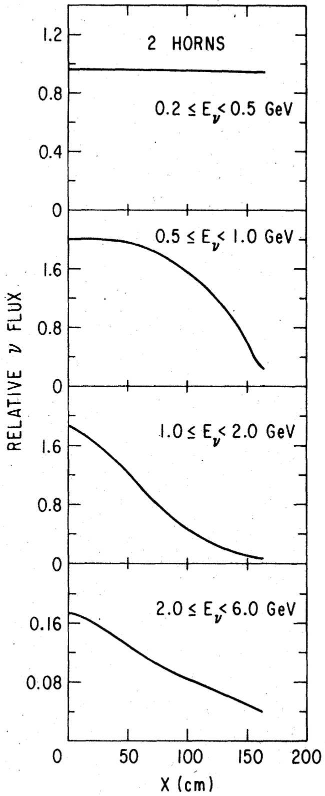

FIG. 6. Radial neutrino flux for different energy selections. For the higher energies, the flux is contained within the bubble chamber.

Since part of the experiment was run with a single horn and part with two horns, we calculated the fluxes separately for the two configurations. Having a substantial number of neutrino interactions, particularly quasi-elastic scattering $\nu d \rightarrow \mu^- p p_s$, whose asymptotic cross section should be independent of neutrino energy, allows us to check the relative effect of the second horn with what we expect and also to check the overall flux shape. This and other checks of the flux that can be made from the data itself are discussed later in the paper.

The ν_e and $\bar{\nu}_e$ flux has also been calculated. There are contributions from charged and neutral kaon and pion decays and, for the lowest energies, μ decays contribute.

Figure 8 shows the overall ν_μ flux with the $\bar{\nu}_\mu$,

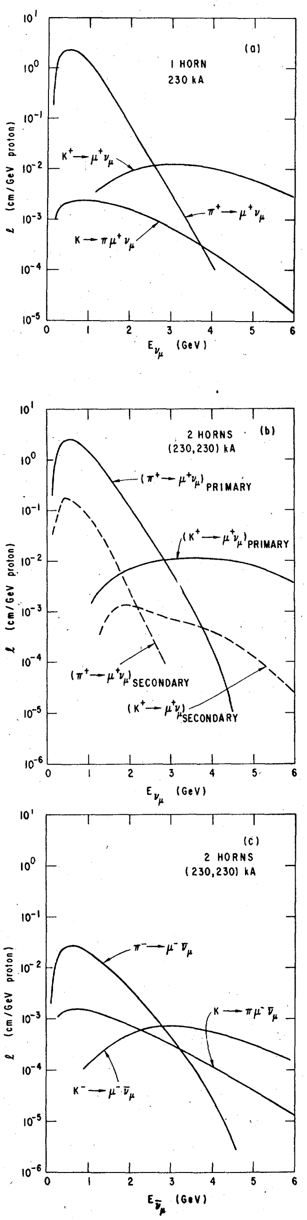

FIG. 7. (a) The neutrino flux for the single-horn case. The different contributions from π and K decay are shown. (b) The neutrino flux for the two-horn case. The dotted lines show the neutrinos coming from the secondary interactions of produced protons. (c) The different contributions to the antineutrino background in the neutrino beam. The units are cm of neutrino pathlength in the bubble chamber.

ν_e, and $\bar{\nu}_e$ backgrounds for the two-horn beam.

Flux uncertainties, both in shape and normalization, are difficult to calculate. We have considered the following factors and assign the errors given when estimating the flux normalization errors:

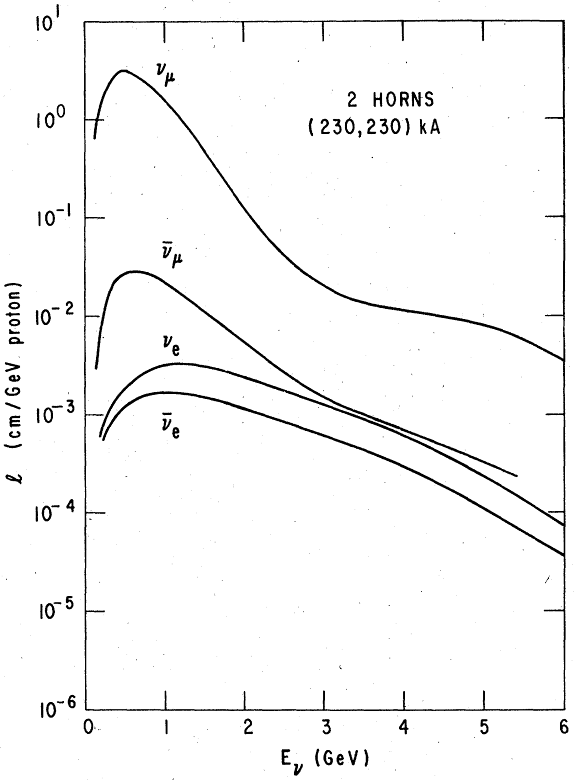

FIG. 8. The ν_μ flux for the two-horn beam with $\bar{\nu}_\mu$, ν_e, and $\bar{\nu}_e$ backgrounds.

(a) errors on the basic π production cross section, ±5%,

(b) uncertainty of the proton beam intensity, ±2%,

(c) distribution of proton beam throughout the target, ±2%,

(d) uncertainty in pion absorption in the target and in the skin of the horn, ±5%,

(e) alignment errors of the horn, ±1%,

(f) uncertainties in tunnel geometry, ±1%,

(g) pion production from protons hitting the front of the muon shield, $+2 \pm 2\%$.

Our estimated overall uncertainty to the flux curve of Fig. 8 amounts to ±15% in the optimum central neutrino energy interval.

III. THE BUBBLE CHAMBER

The bubble chamber, the cross-section view of which is shown in Fig. 9, is an upright cylinder about 2 m high and 3.6 m in diameter.[23] The visible volume of ~16 m^3 is defined by panels covered with Scotchlite reflecting material to illuminate the bubbles. The total volume of the chamber is 26.3 m^3. Track sensitivity is achieved by pulsed lowering of the bottom of the chamber by about 2 cm. A typical pressure trace is shown in Fig. 10.

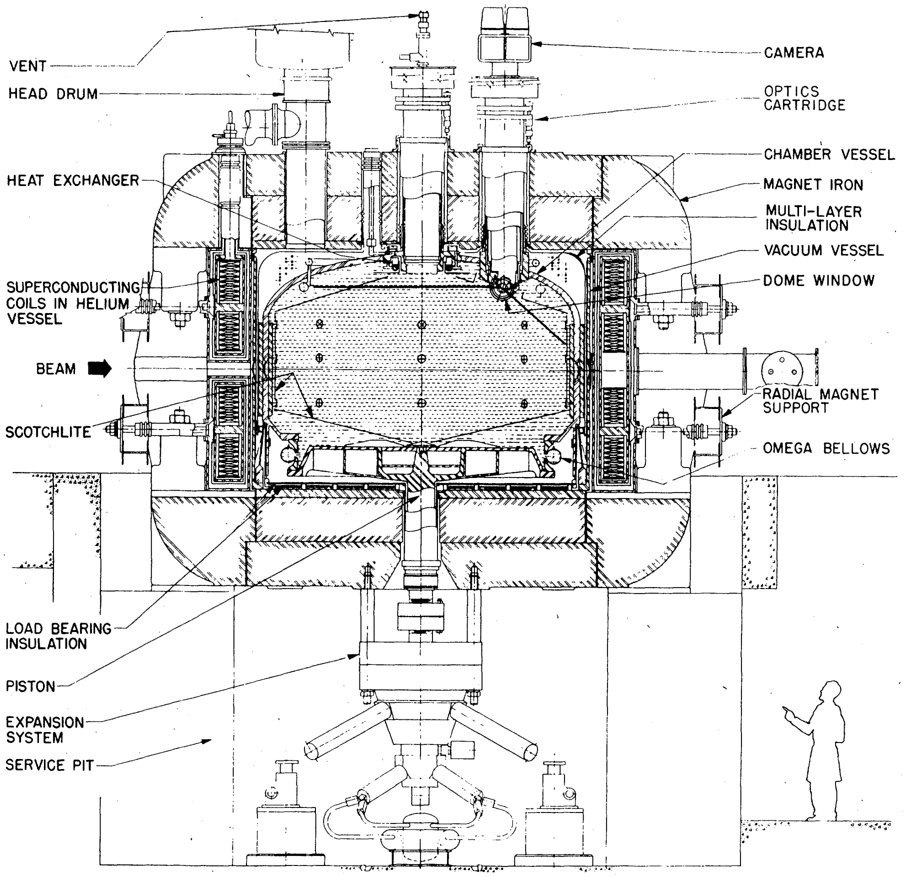

FIG. 9. Cross section of the 12-foot bubble chamber.

This bottom piston is attached to the chamber body by an omega bellows, so that after filling, the chamber volume is completely sealed. The tracks are photographed by four cameras arranged in a square pattern above the sensitive volume, the beam traveling parallel to one side. The image is recorded on a circle 60 mm in diameter on 70-mm perforated film. Because of the lens design, straight lines in space can appear curved on film so that two wires stretched across the chamber in the direction of the beam are useful for showing the local beam direction in any view.

A total of 24 fiducials are mounted on the chamber inner surface and are used to establish the chamber coordinate system. The origin of the coordinate system is equidistant from the four camera lenses, with the negative z axis pointing

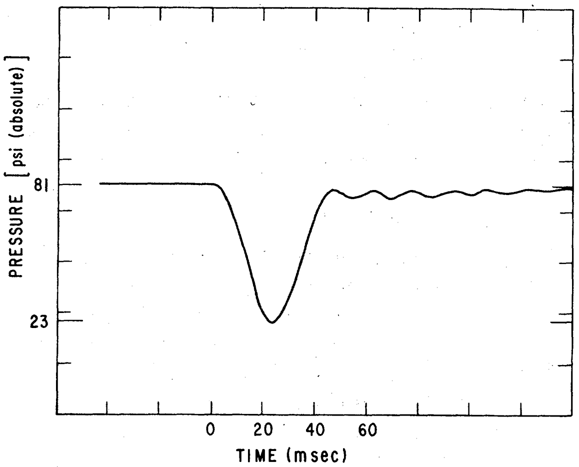

FIG. 10. Pressure wave in the bubble chamber.

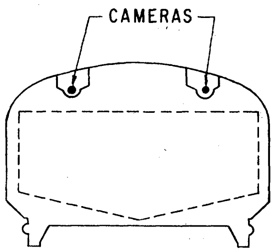

FIG. 11. Schematic cross section of bubble chamber with outline of the fiducial volume.

TABLE I. Bubble-chamber thermodynamic conditions.

	H_2	D_2
Chamber static pressure [psi (absolute)]	68	80
Vapor pressure [psi (absolute)]	58	70
Temperature (°K)	26.1	30.3
Expanded pressure [psi (absolute)]	16	20
Liquid density ($g\,cm^{-3}$)	0.0624	0.142
Volume change in expansion (%)	0.45	0.47

downward perpendicular to the camera plane, and the x and y axes forming a right-handed system with the beam along the x axis. The camera lens pupils are at $z=-24$ cm, and the entire volume with $z<-50$ cm is in focus for all cameras. The nominal beam plane is at $z=-132$ cm. The outline of the fiducial volume of 11 m^3 is shown as the dotted line of Fig. 11, which shows the outline of the chamber vessel. It allows 15 cm of track length between the edge of the fiducial volume and the Scotchlite. For the quasielastic events only, we use a volume of 10 m^3 obtained by restricting the radius of the fiducial region.

The magnetic field is provided by superconducting coils and has a nominal value of 18.0 kG, although the early exposures were taken with a field of 15.5 kG to minimize strains resulting from a vibration problem in the chamber. The field is represented by polynomial expansions in terms of the space coordinates and can be reproduced to within 0.1% over the entire fiducial volume.

The repetition rate of the accelerator during the exposures varied from 1.9 sec to 3 sec, but most pictures were taken with a 2.7-sec repetition rate. Typical thermodynamic conditions of the hydrogen and deuterium are given in Table I.

Six separate exposures of the bubble chamber to the neutrino beam have been made. The details are given in Table II. Notice that the second horn was only used with the last two deuterium exposures and for the deuterium III exposure, the reliability of the second horn was poor. We therefore do not use the data from this exposure in determining the axial form factor. For the first deuterium exposure, three different horn currents were used. A total of 364 000 pictures were taken with a hydrogen filling and 903 000 with a deuterium filling.

IV. SCANNING AND MEASURING

The rate of neutrino interactions in the chamber varied from 1 event every 4000 pictures for the first hydrogen exposure to 1 event every 500 pictures for the last deuterium run. In addition, there were several cosmic-ray tracks on each frame, a small fraction of which gave some kind of an interaction. Other backgrounds came from incident charged hadrons that scattered in the liquid and incident neutrons giving a proton recoil that, in turn, scattered to give a two- or three-pronged event. We therefore did the scanning in two stages. First, an overall scan was made looking for events of any kind. This was usually done with two views projected to about one-seventh life size. The scanners were instructed to record the position of all events that were visible in two or more views and that had two or more prongs. The actual size of the event had to exceed a certain minimum in order to exclude low-energy proton-proton scatters. For each event found, any associated e^+e^- pairs or V^0's were recorded and the

TABLE II. Summary of ν exposures.

Liquid	Frames	Total no. of protons	⟨Protons/pulse⟩	Field (kG)	⟨Current⟩ (kA) Horn I	Horn II
H_2 I	67 000	0.63×10^{17}	0.94×10^{12}	15.0	250	0[a]
H_2 II	296 596	3.134×10^{17}	1.057×10^{12}	15.0	250	0[a]
D_2 I	298 221	4.332×10^{17}	1.453×10^{12}	15.0	~230[b]	0[a]
D_2 II	277 278	3.844×10^{17}	1.386×10^{12}	15.0	232	0[a]
D_2 III	134 757	1.487×10^{17}	1.10×10^{12}	18.0	230	234[c]
D_2 IV	192 784	3.146×10^{17}	1.63×10^{12}	18.0	227	229

[a] Horn 2 was not in place during these runs.
[b] The horn was run at 248, 202, and 232 kA.
[c] Horn 2 was off for $\sim\frac{1}{3}$ of this run.

track characteristics were examined for decays or further interactions. Tracks stopping in the liquid without decaying were noted. Tracks leaving the walls or bottom of the chamber could be identified by the lack of stereo shift and, for most cases, also by the disappearance of the halo around the track at the exit point. A sagitta check was made on all negative tracks to discriminate against protons traveling inwards to the vertex. In addition, all one-prong events were recorded that had the following features:

(a) at least one end of the track was in the liquid, and

(b) the track decayed $\pi \rightarrow \mu \rightarrow e$ or $\mu \rightarrow e$, or

(c) a converted e^+e^- pair pointed to one of the one-prong track, or

(d) the track left the chamber wall or bottom and had more than a minimum length of 2 cm on the scan table, or

(e) the track was positive and stopped in the liquid after more than 7 cm on the scan table.

The scanning rate was typically 85 frames/hour.

Following the scan, an edit was done by an experienced scanner in which all four views of the event were examined on a table that provided a life-size projection as well as the lower magnification image, and the final classifications were made. About 10 times more events were found on the scan than were finally classified as neutrino interactions.

The scanning rules were modified slightly as the experiment progressed and, in particular, for the D_2 I exposure, the one-prong events were not recorded. For all of the D_2 IV exposure and most of the D_2 III, one-pronged events leaving the top of the chamber were recorded in addition to those leaving the sides and the bottom.

All the film has been scanned at least twice. The scanning efficiencies, which were measured for each final state separately, were typically >95%. They are discussed when the physics results for each final state are given.

The events were measured on the semiautomatic machine POLLY.[24] After one pass on POLLY, the remaining events which could not be reconstructed were measured on manual measuring machines. Because of the large size of the bubble chamber and the low average energy of the events, the tracks often traverse many turns before leaving the chamber or interacting. In addition, many track images curve sharply or have cusps on them. Measurements were terminated after the track image had turned by about 60°, and track views having a cusp or other pathological shape near the vertex were not measured.

Reconstruction was done using a modified version of the program TVGP.[25] The point reconstruction accuracy is about 300 μ in the median plane. The track errors are dominated by Coulomb scattering, since most of the particles are of low momentum. Figure 12(a) shows, as an example, the distribution in $\Delta p/p$ as a function of momentum for the π^+ track from the $\nu p \rightarrow \mu^- p \pi^+$ events. The distributions of the errors in azimuth ($\Delta\phi$) and dip ($\Delta\lambda$) for the same track are shown in Figs. 12(b) and 12(c), respectively. Because of the large stereo angle, the dip and azimuthal errors

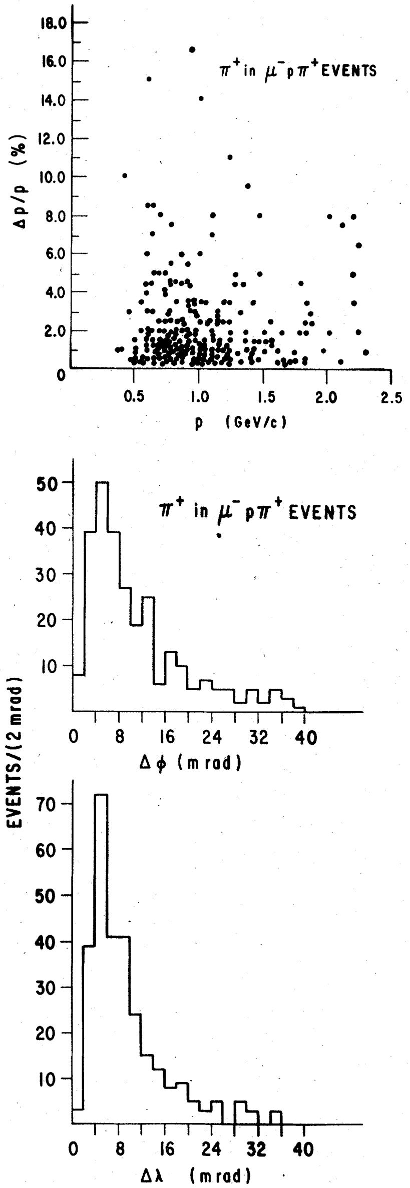

FIG. 12. (a) Momentum errors for π^+ tracks from the reaction $\nu p \rightarrow \mu^- p \pi^+$. Error on (b) azimuth ($\Delta\phi$), (c) dip ($\Delta\lambda$) for π^+ tracks from the reaction $\nu p \rightarrow \mu^- p \pi^+$.

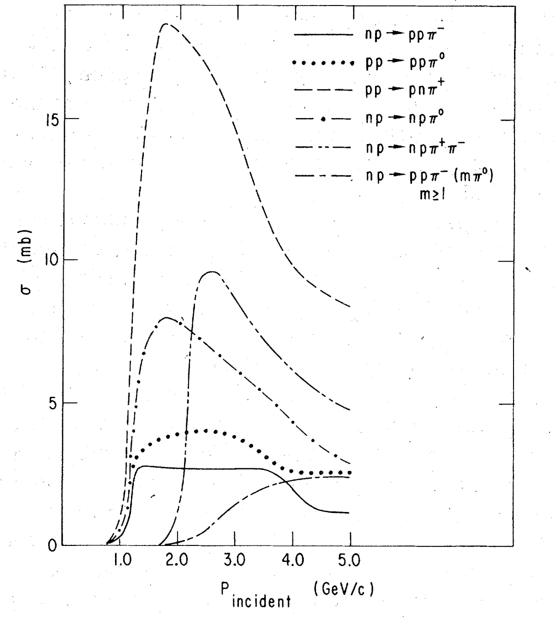

FIG. 13. Some cross sections for *pp* and *np* reactions.

are comparable. The beam direction is $\lambda = \phi = 0$ and downward-going tracks have $\lambda < 0$.

V. NEUTRON BACKGROUND

The neutron flux incident on the bubble chamber can be measured by the spectrum of recoil protons coming from *np* elastic scattering. Above about 1 GeV/*c*, the inelastic reaction $np \rightarrow pp\pi^-$ provides a direct measure of the momentum spectrum and angular distribution of the incident neutrons. The statistical precision, however, is limited.

All three-prong events were tried as one-constraint (1C) fits, assuming the reaction to be $np \rightarrow pp\pi^-$. For the hydrogen filling of the chamber, the fits can be simply made, the only ambiguity occurring for high-momentum incident neutrals where the events of the reaction $\nu p \rightarrow \mu^- p\pi^+\pi^0$ can simulate the $np \rightarrow pp\pi^-$ reaction for cases where neither positive track can be identified as a proton and the negative particle leaves the bubble chamber without interacting or decaying. With a deuterium target, a special problem arises in that there is an ambiguity between events of the reaction $nd \rightarrow pp\pi^- n_s$ and $nd \rightarrow np\pi^- p_s$ when the spectator proton has high momentum. As can be seen in Fig. 13, the cross section for the $np\pi^+$ final state, which is charge conjugate to $pn\pi^-$, is much larger than that for the $pp\pi^-$ due to the pure $I = \frac{3}{2}$ $n\pi^-$ system in the final state. Thus, certain additional criteria must be used for selecting true $pp\pi^-$ events in deuterium. To this end, we require that the χ^2 probability of the fit be >5% and the proton momenta be >250 MeV/*c*. We have checked the corrections on these selection criteria by exposing the bubble chamber with a hydrogen filling to a low-momentum neutron beam and looking at the characteristics of the $np \rightarrow pp\pi^-$ events using a sample of about 100 such fits in the neutron momentum range of 1–3 GeV/*c*.

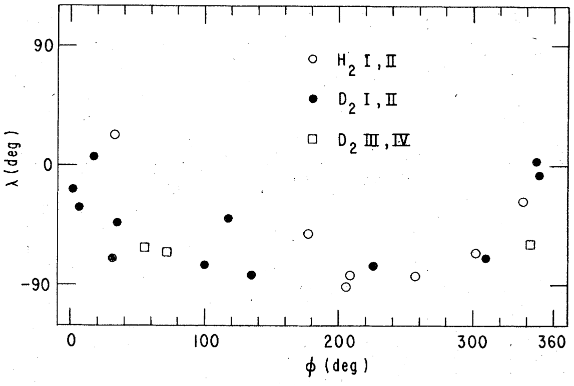

FIG. 14. Distribution in dip (λ) and azimuth (ϕ) for neutrons that undergo the reaction $np \rightarrow pp\pi^-$. The ν beam direction is $\lambda = \phi = 0$. Negative λ corresponds to downward-going particles.

TABLE III. Neutron background.

	Number of $pp\pi^-$ events	Number of $pp\pi^-$ events normalized to integrated proton beam intensity
H_2 I, II	6	1.6 ± 0.7
D_2 I, II	12	1.5 ± 0.5
D_2 III, IV	3	0.6 ± 0.4

Table III gives the number of $pp\pi^-$ events found, grouped into the H_2 and D_2 exposures, the latter in two subgroups. Between each exposure the shielding both near the horn target and around the bubble chamber was improved, mainly by adding more concrete, steel, and sand around the decay tunnel. As a result, the neutron background was improved by a substantial factor for the last two exposures as measured by the number of one-prong events normalized to the number of protons incident on the horn target. The rate of $np \rightarrow pp\pi^-$ events also decreased for the last exposures as seen in Table III. Figures 14 and 15 show the characteristics of the neutrons producing the $pp\pi^-$ final state. It is clear that almost all the neutrons are dipping downwards ($\lambda < 0$), many with steep angles. As seen in Fig. 9, there are five penetrations through the top surface of the magnet iron for the cameras and various plumbing lines. Otherwise, the chamber is surrounded by the thick iron shield of the magnet yoke, so having the main flux of neutrons coming downwards is understandable. The neu-

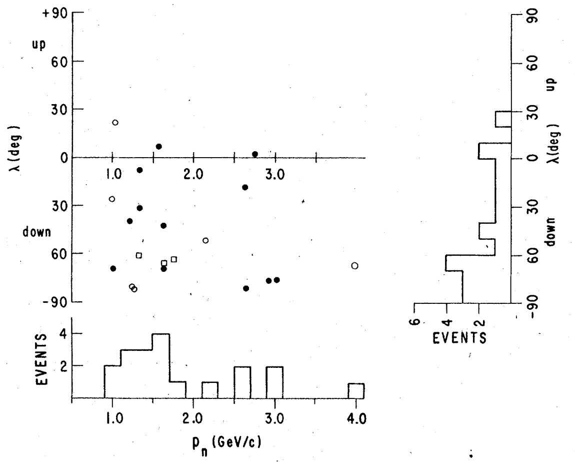

FIG. 15. Distribution in dip (λ) and momentum (P_n) for neutrons that undergo the reaction $np \rightarrow pp\pi^-$.

trons are spread over all azimuthal angles, although there is a slight clustering along the beam direction.

We have estimated the neutron flux above pion threshold resulting from the equilibrium neutrino interactions in the shield and find that less than one $pp\pi^-$ event can come from this source. This number is small because a large fraction of the nucleons resulting from neutrino interactions at our energy are of low momentum and below pion threshold.

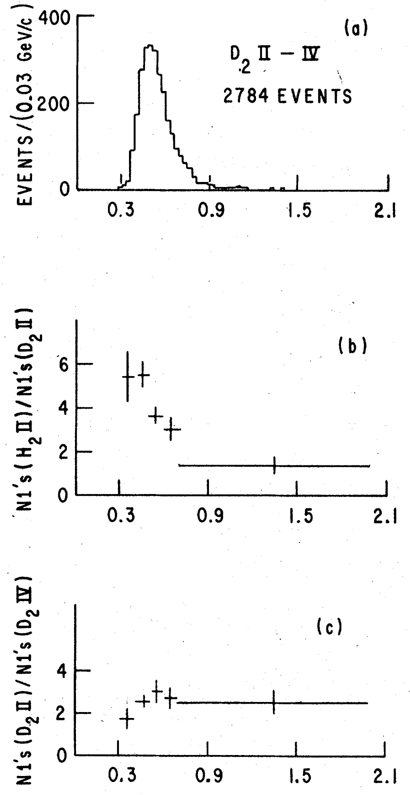

FIG. 16. (a) Proton momentum spectrum for one-prong events from the later deuterium exposures. (b) and (c) show the normalized ratios of one-prong events for different exposures. The reduction in neutron background for the later exposures can be seen.

The spectrum of low-momentum neutrons can be deduced by measurement of the elastic events $np \rightarrow np$. One-prong events were not recorded in the scanning of the D_2 I exposure, so this information is not complete. Figure 16(a) shows the proton momentum spectrum for all leaving protons in the last three D_2 exposures of the chamber. The falloff at low momentum comes about since the tracks are only recorded if they leave the chamber. A calculation of the neutron spectrum that would reproduce the proton spectrum of Fig. 16(a) gives a flux varying as $P_n^{-4.5}$. The reduction in the neutron flux, achieved by the improved shielding, is shown in Figs. 16(b) and 16(c) as ratios of the normalized number of protons for various runs as a function of proton momentum.

The angular distribution of the protons is a reasonable measure of the neutron angular distribution because of the strong charge-exchange peak in the np elastic scattering angular distribution at these energies. The azimuthal angle ϕ', around the neutrino beam direction, is defined in Fig. 17(a). Figure 17(b) shows the distribution in ϕ'

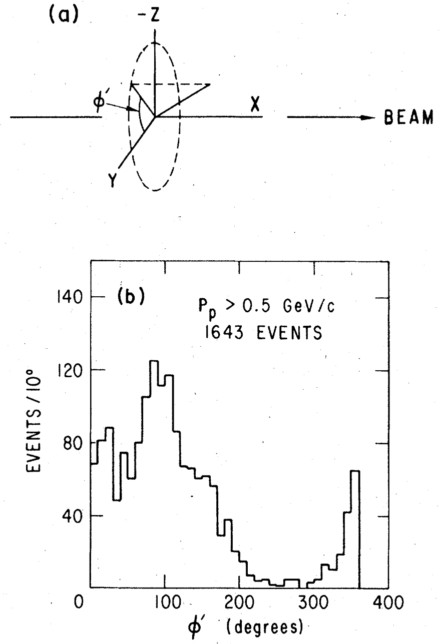

FIG. 17. (a) Definition of azimuthal angle (ϕ') of neutrons that undergo np elastic scattering. (b) Distribution in ϕ' for protons coming from np elastic scattering.

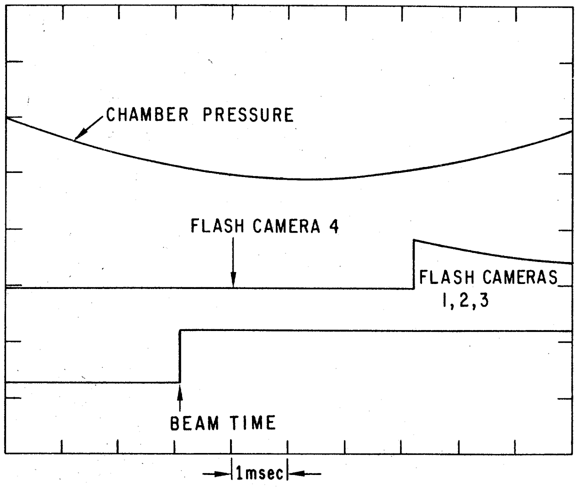

FIG. 18. Chamber-pressure wave and timing of the flash on camera 4 and cameras 1, 2, and 3.

for the D_2 III and IV exposures, and for protons with momentum >500 MeV/*c*. There is a strong depletion of events in which the proton is traveling upwards in the chamber near $\phi' = 270^\circ$, in agreement with the conclusions from the analysis of the $np \to pp\pi^-$ events.

For the later exposures of the chamber, some time discrimination against cosmic-ray events was obtained by timing the flash on camera 4 somewhat earlier than cameras 1, 2, and 3 as shown in Fig. 18. The timing on camera 4 was arranged so that events originating at the beam time were faint but just visible. In this way, any event not visible at all on camera 4 could be rejected as having originated after the beam time and any event having the same appearance on camera 4 as the other three could be rejected as originating significantly earlier than the beam time.

VI. QUASIELASTIC SCATTERING

In order to study the reaction $\nu n \to \mu^- p$, one of course needs a target that contains neutrons. The early experiments[26] were done using a small bubble chamber with either a Freon or a propane fill, resulting in the need to understand the nuclear effects that strongly influence the data, particularly for small momentum transfers. Spark-chamber experiments[4] also had similar problems as aluminum or iron were used as targets. In addition, the spark-chamber experiments had much worse momentum accuracy than is possible with the bubble chamber. The details of the vertex can also be seen in the bubble chamber, and this allows a somewhat better separation of inelastic background. A review of the early experiments is given in Ref. 27.

An analysis of a few hundred ν_μ and $\overline{\nu}_\mu$ quasielastic scattering events from Freon (CF_3Br) has been made using pictures taken in Gargamelle.[28] Here, in addition to the Q^2 shape and the total cross sections for the ν_μ- and $\overline{\nu}_\mu$-induced quasielastic events, one can look at the difference between the differential cross section for the two samples. This difference measures M_A directly through the *V-A* interference term. The result of the Gargamelle experiment is given in Table V together with the other experiments done using complex nuclear targets. The errors are statistical only, except for those of Ref. 28 and Holder *et al.*, Ref. 4, which include flux uncertainties.

Deuterium provides the simplest neutron target, but even here corrections must be made for effects due to Fermi motion, the Pauli exclusion principle, and the exact form of the deuteron wave function. However, these effects are relatively well understood and can be calculated at the few percent level.

Results of our analysis[9] of the first sample of quasielastic scattering events,

$$\nu d \to \mu^- p p_s, \qquad (3)$$

have been published previously. We now give the final results of an analysis of a data sample over three times larger. In addition to our experiment, there is at present only one other experiment using a deuteron target done in the 7-foot chamber at Brookhaven National Laboratory.[29]

A. Selection of events

Events due to reaction (3) are observed in the bubble chamber in the 1-, 2-, or 3-prong topologies, depending on how many protons are visible. One-prong events were not analyzed as the background from hadronic interactions such as *np* elastic scattering is very high. This selection results in a loss of events at low Q^2 and a correction must be made when calculating the energy dependence of the cross section. To make a clean cut, we excluded the region of $Q^2 \leq 0.05\ (\mathrm{GeV}/c)^2$ when studying the form factors. This corresponds to a 4-cm-long recoil proton in the bubble chamber, and so is conservative. In this chamber, one resolves protons with momenta ≥ 100 MeV/*c*, and so when the spectator proton has a momentum greater than this value, a quasielastic scattering event will, in general, be observed as a three-prong event.

In order to ensure enough track length for a reliable measurement, a fiducial volume with a radius of 162 cm was chosen for the quasielastic events only. The volume within this radius is 10 m^3, and it allows a minimum of 25 cm of track between the edge of the fiducial volume and the Scotchlite pan-

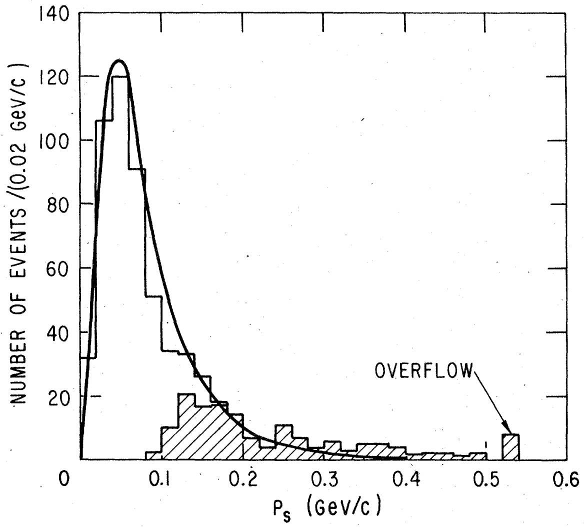

FIG. 19. Spectator momentum distributions for events fitting $\nu d \to \mu^- p p_s$. The shaded area represents the events with a visible spectator. The curve is the Hulthén wave function normalized to the total number of events.

els. With this restriction, we have a sample of 603 events that fit reaction (1) with χ^2 probability >1.0%.

All two- and three-pronged events found were processed through the TVGP and SQUAW programs which performed the geometrical reconstruction and kinematic fitting, respectively. Since the incident neutrino direction is known to within 1°, a three-constraint fit can be performed for reaction (3); the only unknown is the incident neutrino energy. For events in which the nonspectator proton scatters close to the vertex so that a momentum measurement cannot be made, a two-constraint fit was performed; about 1% of the events fall into this category.

For two-prong events, with an unseen spectator, starting values of 0 ± 50 MeV/c were assigned to the Cartesian components of the spectator's momentum. Figure 19 shows the resulting spectator momentum distribution for the events fitting the $\mu^- p p_s$ final state. The shaded area corresponds to seen spectator tracks. The curve is the prediction of a Hulthén wave function (area normalized) and is seen to fit the data well except at the highest momenta, where the data lie above the curve. For $p_s > 200$ MeV/c, the excess amounts to 6%. One normally attributes this excess to rescattering effects. If this is the case then there should be no effect upon the total cross section nor on the calculated values of E_ν and Q^2.

The overall scanning efficiency for the final sample of quasielastic events was 98.5 ± 1%.

Even though a three-constraint fit has been performed to select the quasielastic events, there are still possible sources of background. These come primarily from the reaction

$$\nu d \to \mu^- p \pi^0 p_s , \qquad (4)$$

but neutron-induced events are also significant. In order to determine the background in the sample, we have studied two kinematic quantities. The first (M) is the mass of the beam particle assuming the final state is $\mu^- p p_s$, defined as

$$M^2 = (E_\mu + E_p + E_{p_s} - M_d)^2 - (\vec{P}_\mu + \vec{P}_p + \vec{P}_{p_s})^2 .$$

The second is a space angle α defined as the angle of the vector sum of the momenta of the charged tracks with respect to the ν beam direction. Figure 20, a scatter plot of M^2 versus α, shows the expected accumulation of the real ν-induced events near the origin. We show the 2- and 3-prong events separately in Figs. 20(a) and 20(b), respectively. It is clear that the kinematics of the 3-prong events provides a tighter constraint than for the 2 prongs. The events with $M^2 \simeq 0$ but large α correspond to hadron scatters. Using these plots and extrapolating the distribution of background events to the origin, we estimate an average total background of (2 ± 2)%.

An independent check of the background contribution from events of reaction (4) has been made. These events give fits to the quasielastic hypothesis (3) provided the π^0 transverse momentum is small enough compared to E_ν so that energy and momentum can still be conserved. To study this contribution, we have taken events of the reaction $\nu d \to \mu^- p \pi^+ n_s$, deleted the π^+ track, and fitted to reaction (3). As a result of this study, we estimate that half of the total background comes from the π^0 production reaction. A similar study of the reaction $\nu n \to \nu p \pi^-$ shows that the contribution to the background from this reaction is negligible.

B. Measurement of the form factors

The matrix element for the hadronic weak current depends on six complex form factors.[30] These are F_V^1, the vector form factor, F_V^2, the weak magnetism form factor, F_V^3, the induced scalar form factor, F_A^1, the axial-vector form factor, F_p, the induced pseudoscalar form factor, and F_A^3, the tensor form factor. In terms of these form factors, the weak hadronic current can be written as

$$J_\lambda^{\text{hadronic}} \propto \gamma_\lambda F_V^1 + \frac{i\sigma_{\lambda\epsilon} q^\epsilon F_V^2 (\mu_p - \mu_n)}{2M} + \frac{q_\lambda F_V^3}{M} + \gamma_\lambda \gamma_5 F_A^1$$

$$+ \frac{q_\lambda \gamma_5 F_p}{M} + \gamma_5 \frac{(P_n + P_p)_\lambda}{M} F_A^3 ,$$

where $q(=-Q)$ is the four-momentum transfer, M is the nucleon mass, and μ_p and μ_n are the anom-

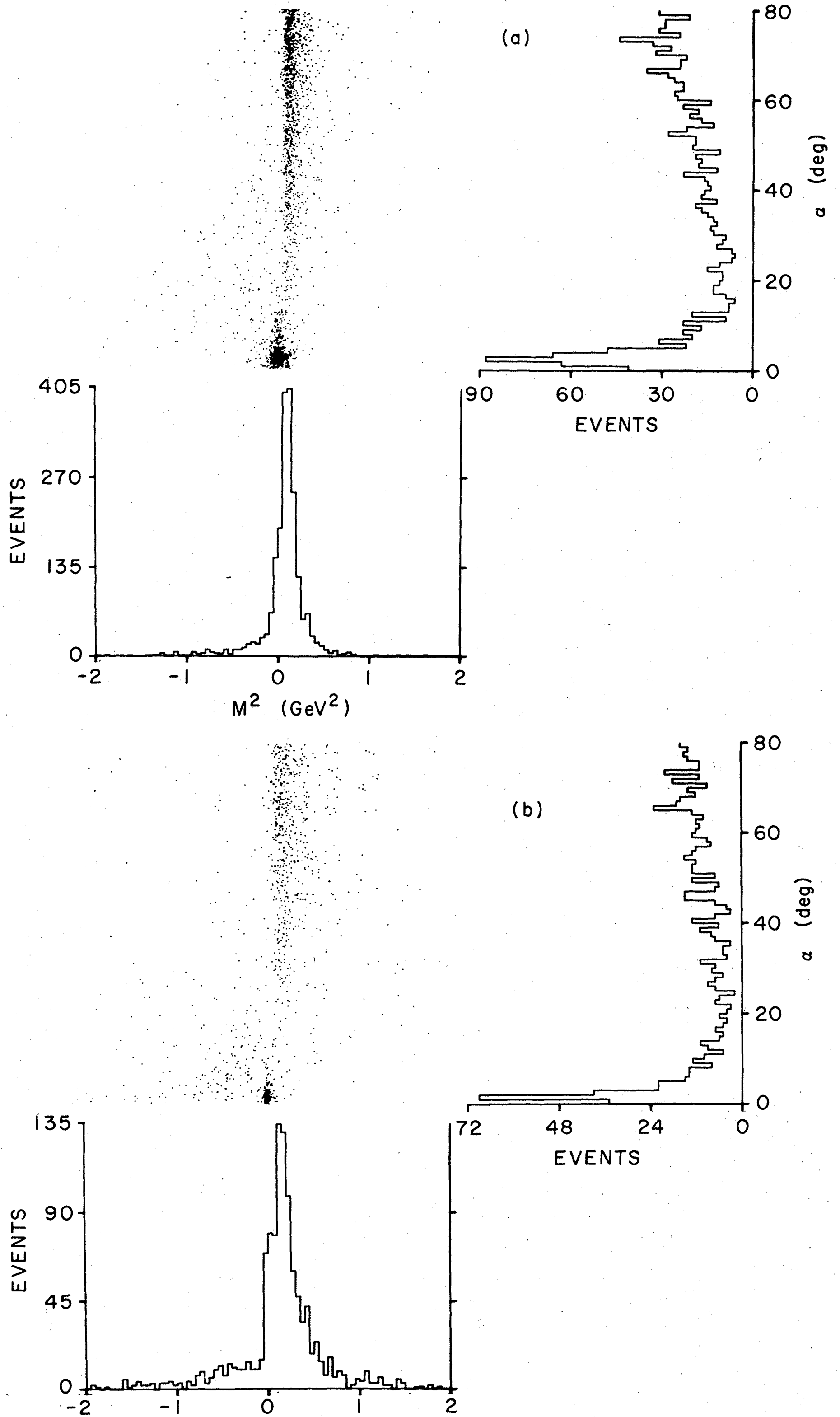

FIG. 20. $M^2{:}\alpha$ distribution for (a) two-prong events, (b) three-prong events fitting the reaction $\nu d \to \mu^- p p_s$. α is the space angle between the ν beam direction and the vector sum of the momenta of the charged tracks, and M^2 is defined as $M^2=(E_\mu+E_p+E_{p_s}-M_d)^2-(\vec{P}_\mu+\vec{P}_p+\vec{P}_{p_s})^2$.

alous magnetic moments of the proton and neutron, respectively.

In order to reduce the problem to a manageable level, certain assumptions must be made. These are as follows:

(*i*) *Time-reversal invariance.* This implies that all the form factors are real.

(*ii*) *Charge symmetry.* As a result F_V^3 and F_A^3 are imaginary. In combination with (i), charge symmetry then requires that $F_V^3 = F_A^3 = 0$. This is equivalent to saying that second-class currents do not exist.

(*iii*) *Isotriplet-current hypothesis.* This assumption relates F_V^1 and F_V^2 to the isovector electromagnetic form factors determined from electron scattering experiments. We use the dipole form and write F_V^1 and $F_V^2 \propto \epsilon(Q^2)/(1+Q^2/M_V{}^2)^2$, where $M_V = 0.84$ GeV, $\epsilon(Q^2)$ is a factor that varies between 0.95 and 1.05 and is used to correct for the deviations of the electron scattering data from a pure dipole.

(*iv*) *Small induced pseudoscalar term.* We assume, following the suggestion of partial conservation of axial-vector current (PCAC), that F_p is dominated by the pion pole. Since the F_p term is multiplied by the muon mass, the contribution to the cross section is small.

(*v*) *Dipole axial-vector form factor.* We take as the parameterization of the axial-vector form factor

$$F_A^1(Q^2) = \frac{-1.23}{(1+Q^2/M_A{}^2)^2},$$

where M_A is a parameter called the axial-vector mass. With the above assumptions, it is the only free parameter.

The cross section for reaction (3) can be written as

$$\frac{d\sigma^\nu}{dQ^2} = \frac{M^2G^2\cos^2\theta_C}{8\pi E_\nu{}^2}[A(Q^2) - B(Q^2)(s-u) + C(Q^2)(s-u)^2],$$

where G is the weak-interaction coupling constant ($GM^2 = 1.023\times10^{-5}$), θ_C is the Cabibbo angle ($\cos^2\theta_C = 0.94$), A, B, and C are functions of Q^2 and the form factors F_V^1, F_V^2, and F_A^1 and $(s-u) = 4ME_\nu - Q^2 - M_\mu{}^2$.

This expression holds for the case of a free neutron and so must be modified in our experiment for the effects of Fermi motion and the Pauli exclusion principle.[31] The corrections will obviously depend weakly on E_ν but strongly on Q^2. Figure 21 shows the factor $R(Q^2)$ by which we multiply the free-neutron cross section in order to correct for the two deuteron effects mentioned.

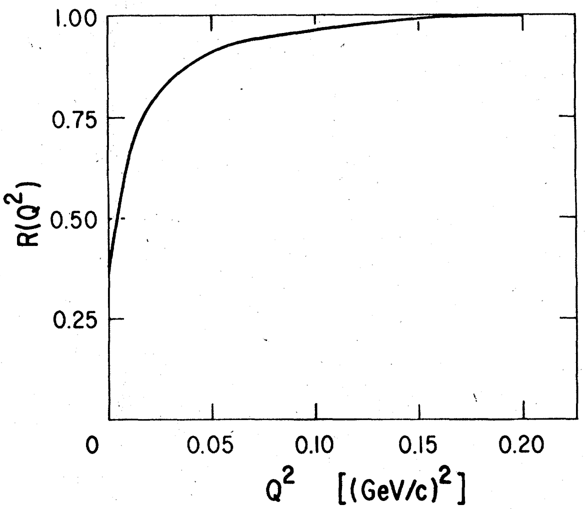

FIG. 21. Correction factor $R(Q^2)$ defined as $R(Q^2) = \sigma(\nu d \to \mu^- p p_s)/\sigma(\nu n \to \mu^- p)$.

Figure 22 shows the total cross section for the quasielastic reaction as a function of E_ν. In calculating the cross section, we have corrected for the region $Q^2 < 0.05$ $(\mathrm{GeV}/c)^2$ and for the Pauli effects and show the cross section for $\nu n \to \mu^- p$ off a free neutron target. As mentioned previously, the flux is known to within ±15% in the region 0.5–1.5 GeV and ±25% elsewhere. These flux uncertainties are added in quadrature with the statistical errors to obtain the errors shown in Fig. 22. As can be seen, the cross section rises to reach a constant value of 0.9×10^{-38} cm^2 at $E_\nu = 0.7$ GeV. This behavior is characteristic of all exclusive channels where the linearly rising cross section is damped by the form factor. The solid curve on the figure is the best fit to the data using a maximum-likelihood method to determine M_A. The dashed lines

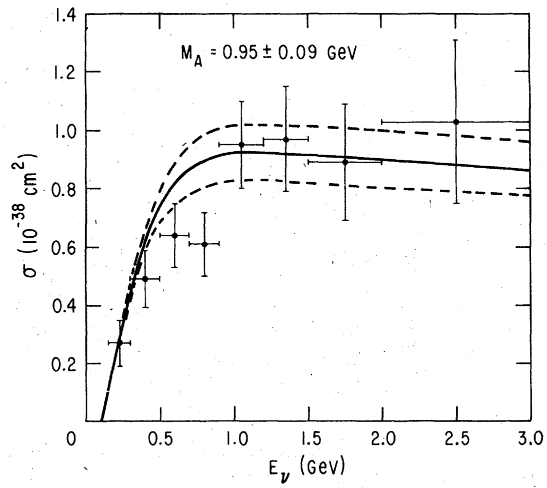

FIG. 22. Total cross section $\nu n \to \mu^- p$ as a function of neutrino energy. The highest-energy data point extends from 2.0 to 6.0 GeV.

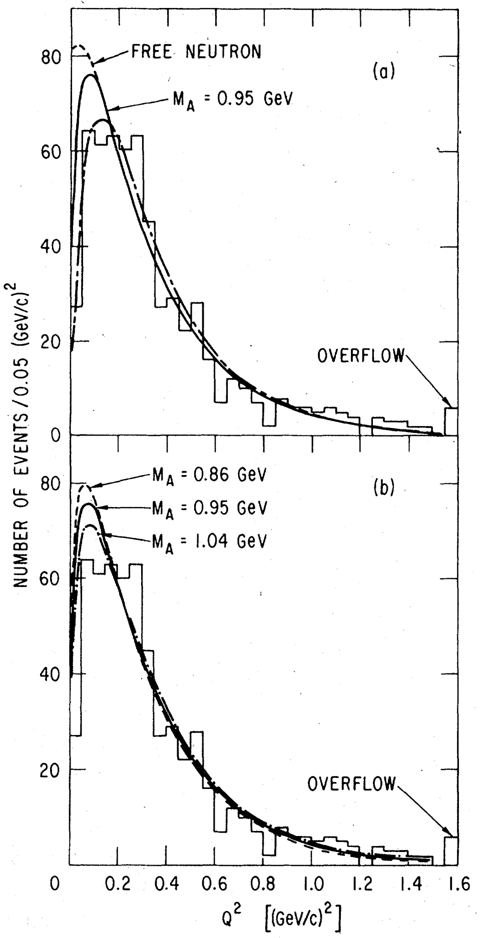

FIG. 23. Distribution of quasielastic scattering events in four-momentum transfer (Q^2). The same data are shown in (a) and (b). The lines on (a) show the best fit for $M_A = 0.95$ GeV for the free neutron case (dotted) and the deuterium case (full line). In (b) the lines show the fits for the three values of M_A shown. In (a) we show in the dashed-dotted curve the prediction for a dipole axial form factor including a second-class axial current with $F_A^3(0) = 7F_A(0)$.

correspond to the one-standard deviation limits of M_A. Note that as M_A increases, the predicted cross section also increases.

In Fig. 23, we exhibit the Q^2 dependence of our data and again show the theoretical prediction. The full curve on Fig. 23(a) includes the deuterium effects and is plotted for $M_A = 0.95$ GeV. The dotted curve shows the expectation for scattering off a free neutron. It must be remembered that there is a depletion of events for $Q^2 < 0.05$ (GeV/c)^2 due to the loss of one-prong events which is not corrected for in Fig. 23. Figure 23(b) shows the data together with three fits for different values of M_A. Note that as M_A increases, the fraction of large Q^2 events also increases. The curve does not follow the data well, particularly for $Q^2 \lesssim 0.4$ (GeV/c)^2, a point to which we return below.

To determine the best value for M_A, we have performed maximum-likelihood fits to the data with $Q^2 > 0.05$ (GeV/c)^2. Four forms of the likelihood functions have been used, and the results are found to be consistent with one another. One form depends only on the total number of events observed and not their kinematic variables and is called the rate term,

$$\mathcal{L}^{\text{rate}} = \frac{1}{(2\pi)^{1/2}\sigma_N} \exp\left[-\frac{1}{2}\left(\frac{N - N(M_A)}{\sigma_N}\right)^2\right],$$

where N is the total number of events observed, $N(M_A)$ is the predicted number of events for a given value of M_A (depending both on the flux shape and magnitude), and σ_N is the error on the expected number of events. This error includes both the systematic flux uncertainty and the statistical error. A second form depends only on the distribution of the events in the (Q^2, E_ν) space and not on the total number. This form depends on the shape of the flux distribution but not on its absolute value and is given by

$$\mathcal{L}^{\text{shape}} = \prod_{i=1}^{N} \frac{\frac{d\sigma}{dQ^2}(Q_i^2, E_\nu^i, M_A)\Phi(E_\nu^i)R(Q_i^2)}{\int\int \frac{d\sigma}{dQ^2}[\Phi(E_\nu)R(Q^2)]dQ^2 dE_\nu},$$

where $\Phi(E_\nu)$ is the ν pathlength (flux) in the energy interval dE_ν at E_ν.

A total likelihood function can be written as the product of the rate and shape terms and is called $\mathcal{L}^{\text{tot}} = \mathcal{L}^{\text{rate}}\mathcal{L}^{\text{shape}}$. In principle, $\mathcal{L}^{\text{tot}}$ provides the most sensitive determination of M_A. A final form, $\mathcal{L}^{FI}$, is totally independent of the flux (both in shape and magnitude) and is given by

$$\mathcal{L}^{FI} = \prod_{i=1}^{N} \frac{\frac{d\sigma}{dQ^2}(Q_i^2, E_\nu^i, M_A)R(Q_i^2)}{\int \frac{d\sigma}{dQ^2}(Q^2, E_\nu^i, M_A)R(Q^2)dQ^2}.$$

The results of the various fits are listed in Table IV. The errors correspond to a change in the likelihood function of ±0.5 units. It is seen that all methods are consistent, and we quote a final value of $M_A = (0.95 \pm 0.09)$ GeV based on $\mathcal{L}^{\text{total}}$. We note that this value and its error are identical to the flux-independent determination based on the shape of the Q^2 distribution only. To determine the goodness of the fit, a Monte Carlo simulation has been performed to determine the distribution for the values of the likelihood function. Based on these calculations, we find that our experiment gives a value of $\mathcal{L}^{\text{tot}}$ better than 10% of all possible experiments with the same statistics. The M_A value measured from the rate is lower than the measurement

TABLE IV. Results of axial-form-factor fits.

Likelihood function	M_A^{Dipole} (GeV)	M_A^{Monopole} (GeV)	M_A^{Tripole} (GeV)
Rate	$0.75^{+0.13}_{-0.11}$	$0.45^{+0.11}_{-0.07}$	$0.96^{+0.17}_{-0.14}$
Shape	1.010 ±0.09	0.56 ± 0.08	1.32 ± 0.11
Rate and shape	0.95 ±0.09	0.52 ± 0.08	1.25 ± 0.11
Flux independent	0.95 ±0.09	0.53 ± 0.08	1.25 ± 0.11

based on the shape, which perhaps reflects the difficulty of absolute neutrino cross-section measurements, a point to which we return in the last section of the paper.

Also in Table IV, we show the results for a monopole and tripole fit. Based on the values of the likelihood functions, one cannot distinguish between the three forms.

As a test of conserved vector current (CVC), one can also allow both M_A and M_V to vary and do a two-parameter fit. Figure 24 shows a contour plot of the $\mathcal{L}^{\text{shape}}$ values in (M_A, M_V) space, where we find a best fit of $M_V = (0.94^{+0.05}_{-0.08})$ GeV and $M_A = (0.77^{+0.27}_{-0.18})$ GeV. Thus, we are consistent with the CVC prediction of $M_V = 0.84$ GeV, and within our errors M_A and M_V are equal.

We have checked the sensitivity of M_A to various selections in the data. These include cuts on E_ν, Q^2, p_s, fiducial volume, event topology, scanning, etc. The results were found to be independent of such selections.

Table V summarizes other measurements of M_A from neutrino interactions using a dipole parameterization. Table VI summarizes the less direct estimates from electroproduction data.[32-36] All the neutrino experiments, except ours and the Brookhaven experiment, were done using complex nuclei as targets. All the bubble-chamber experiments are consistent with one another, and the weighted average value for all bubble-chamber experiments is $M_A = (0.90 \pm 0.06)$ GeV.

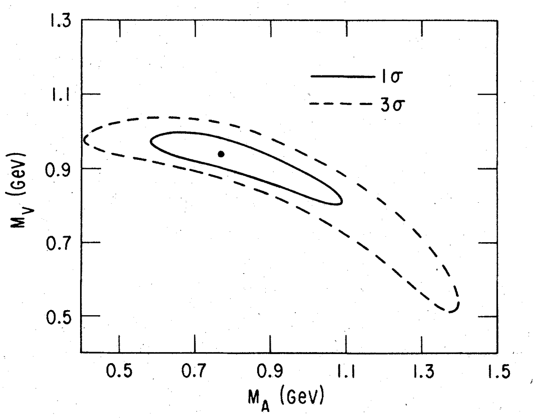

FIG. 24. Likelihood contours in M_A-M_V space.

The electroproduction experiments use PCAC and current algebra in the limit of zero pion mass to determine M_A. However, extrapolation must be made to the correct pion mass, and these corrections are quite model-dependent. This is less true for the reaction $e^- p \to e^- \pi^- \Delta^{++}$. In Table VI the results are given for different methods of extrapolation. Based on the Dombey-Reed (DR) model, the average value of M_A is found to be 1.13 ± 0.03 GeV, whereas the Benfatto, Nicolo, and Rossi (BNR) technique gives an M_A value of 0.99 ± 0.02, in agreement with the neutrino experiments. Other extrapolation techniques have been used by Nambu and Yoshimura (NY), Adler and Weissberger (AW), and Furlan, Paver, and Verzegnassi.[37]

As noted above and seen in Fig. 23, the data from our experiment do not follow the expected shape in four-momentum transfer. Although the number of events is not yet sufficient to unambiguously establish a discrepancy, it is interesting to speculate on possible origins of the effect. The simplest explanation is that the axial form factor is not a dipole. It is well known that the proton magnetic form factor deviates from the simple dipole shape,[38] as shown in Fig. 25(a). We find that we can reproduce the neutrino data of Fig. 23 by a modification of the axial form factor from a dipole by the factor shown in Fig. 25(b).

A second, but much less likely, possibility is that the second-class axial current is not zero. The momentum transfer distribution can also be reproduced by introducing such a term. We show as an example the predicted Q^2 shape by the dot-dashed line on Fig. 23(a). This is calculated with $F_A^3(0) = 7F_A(0)$. We also assumed the second-class form factor has a dipole shape in Q^2 with M_{A_3}

TABLE V. Measurements of M_A using neutrino beams.

Target	M_A (GeV)	Reference
d	0.95 ± 0.09	This expt.
CF_3Br	$1.0^{+0.50}_{-0.35}$	5
C_3H_8	0.7 ±0.2	26
CF_3Br	0.96 ± 0.16	28
d	$0.76^{+0.14}_{-0.40}$	29
Al	$0.60^{+0.55}_{-0.35}$	4
Fe	1.05 ± 0.2	

TABLE VI. Measurements of M_A using electroproduction data.

Pion extrapolation method	M_A (GeV)	Reference
DR	1.14 ±0.09	32
NY	1.521±0.064	33
DR	1.12 ±0.03	34
DR	1.06 ±0.06	35
AW	1.18 ±0.07	36
BNR	1.02 ±0.04	32
BNR	0.96 ±0.03	34

= 0.8 GeV. Such a large second-class axial current has been suggested by some nuclear physics experiments.[39] A similar effect on the Q^2 distribution can be produced if CVC is violated in the sense that the normalization of the weak magnetism term F_V^2 is not given by $(\mu_p - \mu_n)/2M$ but is much larger.

VII. CHECK OF NEUTRINO FLUX FROM THE QUASIELASTIC SCATTERING EVENTS

The cross sections, shown in Fig. 22, are calculated using the flux measured from our pion production cross sections. If we assume a value for M_A, then we can, in turn, use the total cross-section data to measure the neutrino flux. Since M_A can be measured from the shape of the Q^2 distribution only, this provides a useful independent measurement of the flux. The M_A value we use is $M_A = 0.95$ GeV, our flux-independent result as given in Table IV, which is also consistent with values obtained by other neutrino experiments listed in Table V. Our event numbers then give a flux that is 21% lower than that measured from our pion yields.[40]

A second technique which is completely independent of the form factors is to extrapolate the differential cross section to $Q^2 = 0$, where the cross section is given by

$$\left.\frac{d\sigma}{dQ^2}\right|_{Q^2=0} = \frac{G^2\cos^2\theta}{2\pi}\left[F_V(0)^2 + F_A(0)^2\right]$$
$$= 1.98\times 10^{-38}\ \text{cm}^2/\text{GeV}^2 .$$

Extrapolating the data of Fig. 23 to $Q^2 = 0$ also gives a flux that is 22% lower than shown in Fig. 8 in agreement with the previous method.

We estimate a ±12% uncertainty in the flux measured from the quasielastic data using a conservative error of ±0.10 GeV on M_A. Averaging this measurement with the flux directly calculated from the pion production cross sections, we estimate that the flux curves (Figs. 7 and 8) are 13% too high. The error on the reduced mean flux is ±10%.

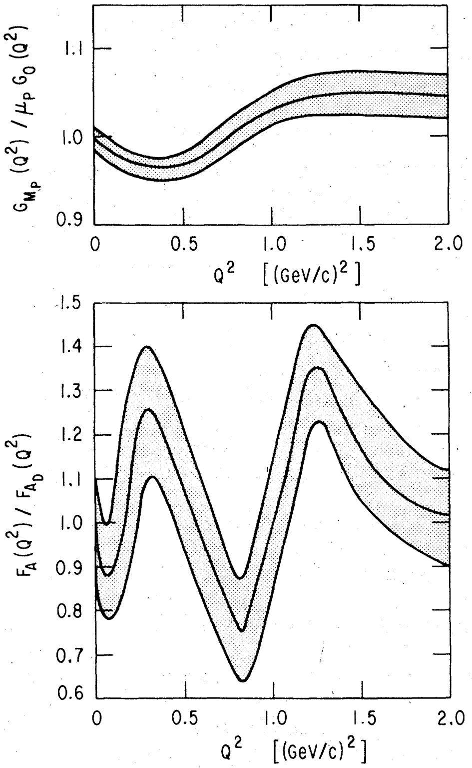

FIG. 25. (a) Deviation of the magnetic form factor of the proton from the dipole form. (b) Deviation of the axial weak form factor of the nucleon from a dipole form assuming no second-class axial currents. The shaded areas roughly represent the errors.

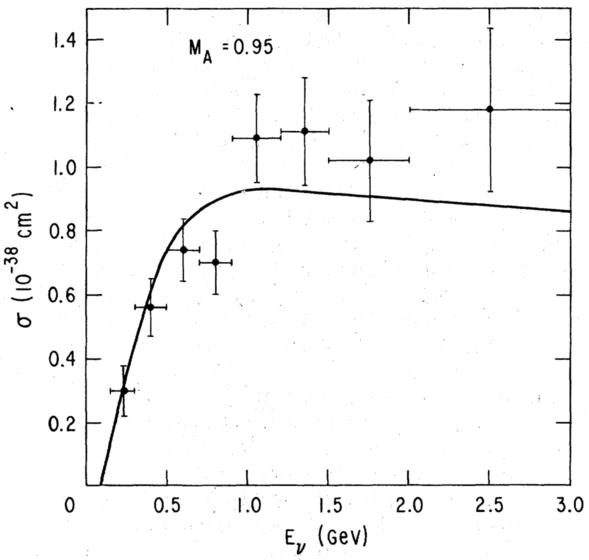

FIG. 26. Cross section for the reaction $\nu n \to \mu^- p$ as a function of neutrino energy. For these data, the normalization has been determined by averaging the flux calculated from the pion production cross sections with the flux obtained using the shape of the measured dN/dQ^2 distribution. The highest-energy data point extends from 2.0 to 6.0 GeV.

Using this new value of the flux, we plot in Fig. 26 our best determination of the cross section as a function of neutrino energy.

ACKNOWLEDGMENTS

This experiment could not have been done without the help of many people at the Zero Gradient Synchrotron. We particularly wish to thank K. Jaeger and A. Thomas for efficient operation of the bubble chamber, W. Praeg for the construction and operating of the horn system, and H. Chafee for organizing the film scanning effort at Argonne.

---

†Work supported by the U.S. Energy Research and Development Administration.

*Present Address: Carnegie-Mellon University, Pittsburgh, Pa. 15213.

‡Present Address: IBM, Gaithersburg, Md. 20760.

§Present Address: U.S. ERDA, Washington, D. C. 20545.

||Present Address: State University of New York, Stony Brook, N. Y. 11973.

¶Present Address: Tufts University, Medford, Ma. 02155.

**On leave from the Institute for Nuclear Research, Warsaw, Poland.

††Present Address: Tohoku University, Sendai 980, Japan.

[1] F. Reines and C. L. Cowan, Phys. Rev. 92, 830 (1953).

[2] M. Schwartz, Phys. Rev. Lett. 4, 306 (1960); B. Pontecorvo, Zh. Eksp. Teor. Fiz. 37, 1751 (1959) [Sov. Phys.—JETP 10, 1236 (1960)].

[3] G. Danby *et al.*, Phys. Rev. Lett. 9, 36 (1962).

[4] M. Holder *et al.*, Nuovo Cimento 57, 338 (1968); E. Hyman, Ph. D. thesis, Columbia University Nevis Report No. 158 (unpublished); R. L. Kustom *et al.*, Phys. Rev. Lett. 22, 1014 (1969).

[5] M. Block *et al.*, Phys. Lett. 12, 281 (1964).

[6] I. Budagov *et al.*, Phys. Lett. 29B, 524 (1969).

[7] P. Queru, in *Proceedings of the International Conference on Bubble Chamber Technology*, edited by M. Derrick (Argonne National Laboratory, Argonne, Illinois, 1970), p. 460.

[8] See, for example, D. H. Perkins, in *Proceedings of the Fifth Hawaii Topical Conference on Particle Physics, 1973,* edited by P. N. Dobson, Jr., V. Z. Peterson, and S. F. Tuan (Univ. of Hawaii Press, Honolulu, 1974).

[9] W. A. Mann *et al.*, Phys. Rev. Lett. 31, 844 (1973).

[10] J. Campbell *et al.*, Phys. Rev. Lett. 30, 335 (1973).

[11] S. J. Barish *et al.*, Phys. Rev. Lett. 36, 179 (1976).

[12] S. J. Barish *et al.*, Phys. Lett. 66B, 291 (1977).

[13] F. Hasert *et al.*, Phys. Lett. 46B, 138 (1973).

[14] S. J. Barish *et al.*, Phys. Rev. Lett. 33, 448 (1974).

[15] H. Vogel *et al.*, *Proceedings of the International Symposium on Magnet Technology, Stanford, California, 1965,* edited by H. Brechna and H. S. Gordon (National Bureau of Standards, U. S. Department of Commerce, Washington, D. C., 1966), p. 650.

[16] E. P. Steinberg *et al.*, Nucl Phys. A113, 265 (1968).

[17] Y. Cho *et al.*, Phys. Rev. D 4, 1967 (1971).

[18] J. G. Asbury *et al.*, Phys. Rev. 178, 2086 (1969); G. Marmer and D. Lundquist, Phys. Rev. D 3, 1089 (1971).

[19] J. R. Sanford and C. L. Wang, BNL AGS Internal Report, 1967 (unpublished); C. L. Wang, Phys. Rev. Lett. 25, 1068 (1970); 25, 1536(E) (1970).

[20] J. Allaby *et al.*, CERN Report No. CERN/Th 70-12 (unpublished).

[21] G. Bellettini *et al.*, Nucl. Phys. 79, 609 (1966).

[22] R. A. Lundy *et al.*, Phys. Rev. Lett. 14, 504 (1965). The cross sections measured by Lundy *et al.* are higher by a factor of about 1.5 than both our results of Ref. 17 and the data of Refs. 18 and 20. We therefore believe that the normalization of the Lundy data is in error.

[23] A. Tamosaitis, in *Proceedings of the International Conference on Bubble Chamber Technology*, edited by M. Derrick (Argonne National Laboratory, Argonne, Illinois, 1970), p. 765.

[24] W. M. M. Allison *et al.*, Nucl. Instrum. Methods 84, 129 (1970).

[25] J. Campbell, in *Proceedings of the International Conference on Bubble Chamber Technology*, edited by M. Derrick (Argonne National Laboratory, Argonne, Illinois, 1970), p. 303.

[26] I. Budagov *et al.*, Lett. Nuovo Cimento 2, 689 (1969).

[27] M. Derrick, in *Proceedings of the Sixth International Symposium on Electron and Photon Interactions at High Energies, Bonn, 1973,* edited by H. Rollnik and W. Pfeil (North-Holland, Amsterdam, 1974), p. 369.

[28] S. Bonetti *et al.*, Nuovo Cimento 38, 260 (1977).

[29] E. Cazzoli *et al.*, paper presented at the 1976 Aachen Neutrino Conference (unpublished).

[30] T. D. Lee and C. N. Yang, Phys. Rev. 126, 2239 (1962); C. H. Llewellyn Smith, Phys. Rep. 3C, 261 (1972).

[31] S. K. Singh, Nucl. Phys. B36, 419 (1972).

[32] E. Amaldi *et al.*, Phys. Lett. 41B, 216 (1972).

[33] E. D. Bloom *et al.*, Phys. Rev. Lett. 30, 1186 (1973).

[34] A. del Geurra *et al.*, Nucl. Phys. B107, 65 (1976).

[35] P. Brauel *et al.*, Phys. Lett. 45B, 389 (1973).

[36] P. Joos *et al.*, Phys. Lett. 62B, 230 (1976).

[37] G. Furlan, N. Paver, and C. Verzegnassi, Nuovo Cimento 63A, 519 (1969); 70A, 247 (1970).

[38] R. Bartoli *et al.*, Riv. Nuovo Cimento 2, 241 (1972).

[39] K. Sugimoto *et al.*, Phys. Rev. Lett. 34, 1533 (1975); F. P. Calaprice *et al.*, *ibid.* 35, 1566 (1975); R. E. Tribble and G. T. Garvey, Phys. Rev. C 12, 967 (1975).

[40] We note that the Lundy data of Ref. 22 give pion production cross sections 50% higher than we measure and, therefore, have a bigger discrepancy with the flux measured assuming a value for M_A. This is also true of the Allaby data of Ref. 20, although in this case the agreement with our data is within 10%.